On Shear-Generated Gravity Waves that Reach the Mesosphere. Part II: Wave Propagation

OLIVER BÜHLER* AND MICHAEL E. McINTYRE

Centre for Atmospheric Science, Department of Applied Mathematics and Theoretical Physics, University of Cambridge, Cambridge, United Kingdom

ABSTRACT

The propagation of Kelvin–Helmholtz (KH) shear-generated gravity waves through the summer stratosphere is investigated using ray tracing, taking into account back-reflection as well as wave dissipation due to precritical-layer breaking, radiative damping, and viscous diffusion. It is found that the transmission rate of upward–eastward waves to the mesosphere is surprisingly good, provided that the horizontal scale of the waves is large enough to prevent back-reflection. A rough upper bound on the net momentum flux into the mesosphere due to a large ensemble of mutually incoherent KH-generated clear-air turbulence events is then estimated, using reasonable-looking assumptions about the statistics of such events. It is found that on this basis the wave source cannot safely be neglected in the global angular momentum budget.

1. Introduction

The formation of a mixed layer of fluid by a clear-air turbulence (CAT) event and the subsequent emission of low-frequency gravity waves from this mixed layer were investigated in the companion paper Bühler et al. (1999, hereafter BMS; cf. stages A and B in Fig. 2 thereof). This paper studies stage C of this sequence, namely the propagation of the emitted waves through a slowly varying mean flow using ray tracing. The ray tracing takes into account the systematic negative mean zonal shear indicated in the summer profile in Fig. 1 of BMS and the dissipation of the waves by radiative damping and viscous diffusion. The effect of the mean shear is that only the upward–eastward part of the emitted gravity wave spectrum is able to propagate vertically to mesospheric altitudes. This leads to a net flux of positive zonal pseudomomentum into the mesosphere despite the fact that the initial pseudomomentum emission is symmetric in positive and negative zonal pseudomomentum.

The upward–eastward waves that are transmitted to the mesosphere will have reduced amplitudes owing to the cumulative effect of wave dissipation during propagation. After consideration of a few sample ray-tracing runs that illustrate the generic behavior of the waves, the net pseudomomentum flux into the mesosphere from a single mixed layer is calculated by ray tracing each spectral component of the emitted waves. Finally, a rough upper bound on the net pseudomomentum flux into the mesosphere due to a large ensemble of mutually incoherent mixed layers is estimated by combining the single-event flux with observed CAT statistics.

2. Stage C in Fig. 2 of BMS: Ray tracing

The ray tracing is done here in two spatial dimensions, that is, zonal direction x and altitude z. The mean flow is modeled as a steady zonal flow $U(z)$ that depends only on the altitude z, and the buoyancy frequency N and Coriolis parameter f are taken to be constant. This model provides a simple first approximation that arguably captures the strongest summertime mean-flow effects. Generalizing these calculations to, say, three spatial dimensions, and varying N, etc., would be more costly computationally, but would otherwise be completely straightforward.

a. East–west filtering by the mean zonal shear

Consider Fig. 1, which shows gravity wave group-velocity rays emitted from the center of a mixed region that is embedded in a mean shear profile (indicated by the broken line). The indicated negative mean shear is

---

* Current affiliation: School of Mathematical and Computational Sciences, University of St. Andrews, The North Haugh, St. Andrews, United Kingdom.

Corresponding author address: Dr. Oliver Bühler, School of Mathematical and Computational Sciences, University of St. Andrews, The North Haugh, St. Andrews KY16 9SS, United Kingdom.
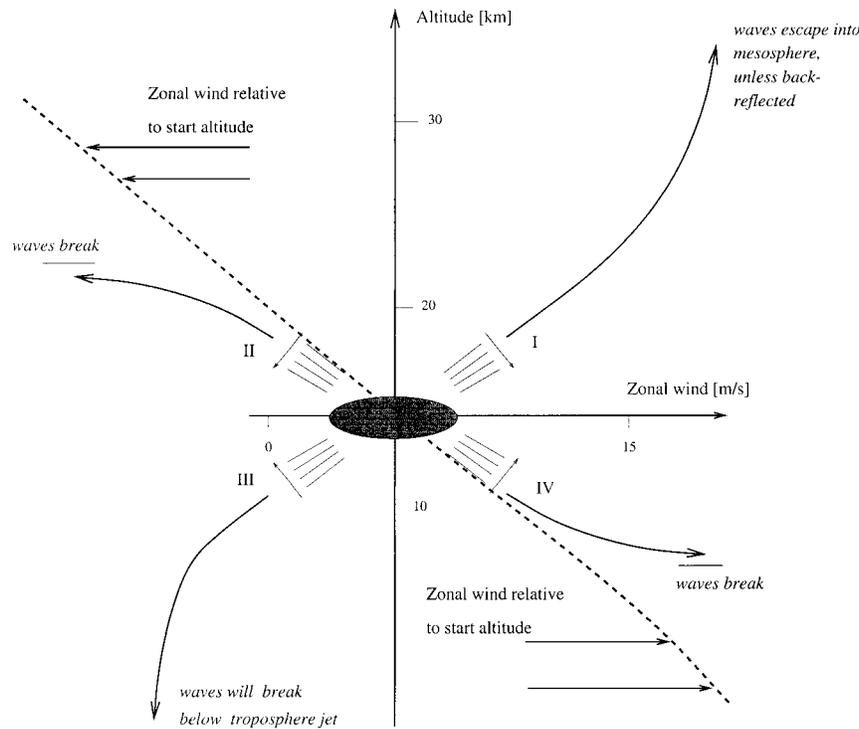E-mail: obuhler@mcs.st-and.ac.uk

FIG. 1. Schematic of the selective transmission of gravity waves by the mean zonal shear. The size of the mixed region is greatly exaggerated. See text for details.

typical for average summer conditions; cf. Fig. 1 in BMS. The vertical axis puts the mixed region at a start altitude of about 15 km, which is a typical altitude just above the tropopause jet. At this altitude the mean zonal velocity is westerly with a magnitude of about 10 m s^{-1}, and the rays are depicted as seen in a frame moving with this mean velocity. (For simplicity of illustration only the intrinsic part of the group-velocity rays is depicted; that is, no effort has been made to show the differential horizontal advection of the waves by the mean wind.)

The background flow field is steady and x independent and hence the absolute wave frequency ω measured by an observer fixed to the earth's surface, as well as the zonal wavenumber k, are constant along rays, that is,

$$\omega \equiv \hat{\omega} + U(z)k = \hat{\omega}_0 + U(z_0)k_0 \quad \text{and} \quad (1)$$

$$k = k_0, \quad \text{where} \quad (2)$$

$$\hat{\omega} \equiv +\sqrt{\frac{N^2 k^2 + f^2 m^2}{k^2 + m^2}} \Rightarrow N \geq \hat{\omega} \geq f. \quad (3)$$

Here $\hat{\omega}$ is the intrinsic frequency along a ray (defined to be positive in accordance with the convention used in BMS), m is the vertical wavenumber, $U(z)$ is the zonal mean wind as a function of altitude z, and the subscript 0 denotes the corresponding initial values of these quantities at the start of the ray. Note that the vertical component m varies along the ray to ensure the invariance of ω.

As is well known (e.g., Lighthill 1978), gravity waves cannot cross heights where Eqs. (1) and (3) become incompatible, that is, where (1) would put $\hat{\omega}$ outside the interval allowed by the dispersion relation in (3). The case $\hat{\omega} \rightarrow N$ is total back-reflection; that is, at such heights the wave packet changes its direction of vertical propagation in finite time. If $\hat{\omega} \rightarrow f$, on the other hand, the wave packet approaches a so-called critical layer. This implies the unbounded growth of wave amplitudes, the breakdown of linear theory, and the general nonlinear breaking of the wave before the critical layer is reached.

The qualitative nature of the development of four typical rays emitted into four different quadrants (I–IV) in Fig. 1 can now be read off from (1) using $k = k_0$. The type-I ray initially goes eastward (to the right in the figure) and upward; that is, it has positive x and z components of intrinsic group velocity, and therefore $k_0 > 0$ and $m_0 < 0$.[1] Satisfaction of (1) in the presence of negative shear and upward propagation clearly implies increasing values of intrinsic frequency $\hat{\omega}$, and hence

---

[1] This uses the convention that $\hat{\omega} > 0$ and hence that the wavenumber vector $\mathbf{k} = (k, m)$ points in the same direction as the intrinsic phase-velocity vector $\mathbf{k}\hat{\omega}/|\mathbf{k}|^2$.
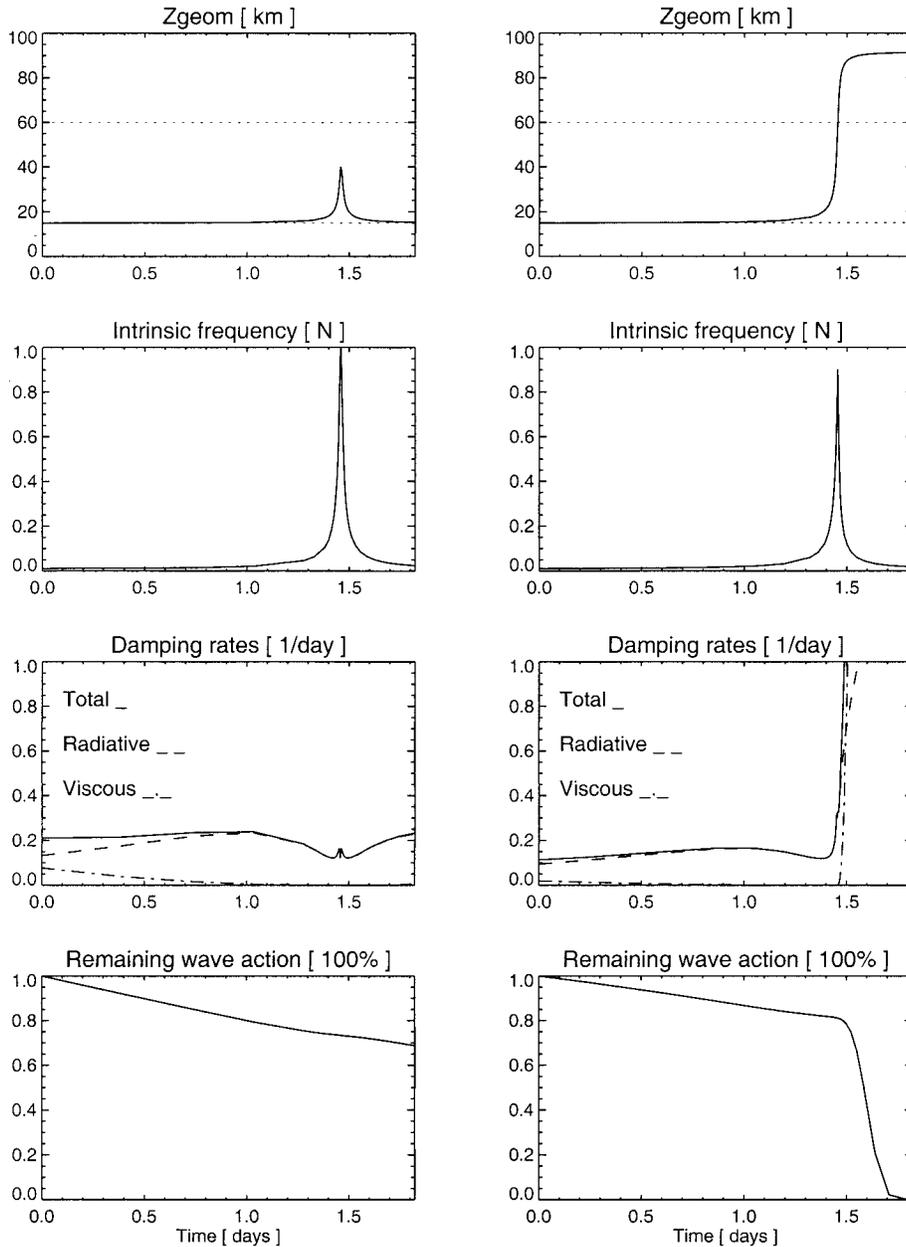
FIG. 2. Ray-tracing results. Rotation $f/N = 1/100$. (left) Packet (a) with $h = 35$ m; (right) packet (b) with $h = 70$ m.

decreasing values of m^2, by (3). Hence type-I waves have their phase-line patterns opened up, the spatial density of their wave crests is decreased, and their vertical group velocity is increased. Unless $\hat\omega$ reaches its upper limit N somewhere on the way up (which is discussed further below) these type-I waves will be able to escape into the mesosphere. The type-II ray goes westward (to the left in the figure) and upward. Hence, it has negative x and positive z components of intrinsic group velocity, and therefore $k_0 < 0$ and $m_0 < 0$. Equation (1) now implies that $\hat\omega$ must decrease, and hence that m^2 must increase. The phase-line pattern is closed

down and if $\hat\omega$ approaches f, then the waves will break. This will in fact invariably happen for the low-frequency waves under consideration here. The emitted spectrum of a flat, pancakelike mixed region with low ratio of height/width $\sim k_0/m_0 \sim f/N$ is dominated by low-frequency inertia-gravity waves with $\hat\omega_0 \sim f$. Therefore, the waves encounter a critical layer at a height $z - z_0$ where

$$|(U(z) - U(z_0))k_0| \sim f \Rightarrow |(z - z_0)m_0| \sim \frac{N}{|U_z|}. \quad (4)$$

Typical values of the background Richardson number

$N^2/(U_z)^2 \lesssim 50$, and hence type-II waves will encounter a critical layer within a few vertical wavelengths from the launch altitude, as indicated in the figure. Hence, there is no escape of type-II waves into the mesosphere. The type-III ray goes westward (to the left in the figure) and downward (i.e., $k_0 < 0$ and $m_0 > 0$). These waves have their phase-line pattern opened up at first in the same way as type-I waves, but then closed down again as they propagate past the tropospheric jet, and will most likely break at some height below the tropospheric jet where the mean velocity drops below $U(z_0)$. In extremely favorable circumstances they might be reflected at the ground and travel upward again, but then they will have turned into a type-II wave and will therefore break near the start altitude. The type-IV ray goes eastward and downward. It breaks near the launch altitude in the same way as type-II waves.

The overall result is that *only* type-I waves might be able to reach the summer mesosphere. The zonal component of pseudomomentum density has the same sign as the intrinsic horizontal phase velocity; and hence type-I waves always transmit *positive* zonal pseudomomentum, which leads to the one-sided, asymmetric momentum flux into the mesosphere noted before. However, only type-I waves with sufficiently large horizontal wavelength $2\pi/k_0$ will evade back-reflection by the easterly jet in the stratosphere. If $\hat{\omega} = N$ is substituted in (1), then the criterion for the absence of back-reflection is

$$k_0 < \frac{N}{\max[U(z_0) - U(z)]} \approx \frac{2\pi}{30 \text{ km}}, \qquad (5)$$

which uses $\max[U(z_0) - U(z)] \cong 70 \text{ m s}^{-1}$, $N \cong 0.015$ s^{-1}, and $\hat{\omega}_0 \sim f \ll N$. Therefore, type-I waves with horizontal wavelength larger than about 30 km evade back-reflection, which implies that waves emitted from larger mixed regions are less affected by back-reflection than waves emitted from smaller mixed regions. Referring back to (25) in BMS, it is clear that these considerations strongly limit the wavenumber section $\mathcal{K}$ that can make contributions to the pseudomomentum radiation into high-altitude regions $\mathcal{D}(t)$.

The criterion (5) can be simply related to the vertical size of the mixed region in BMS's emission model. For that model the location in the spectral plane of the bulk of the emitted pseudomomentum can be read off from Fig. 5 in BMS as $kH \approx 0.01$, where H is the vertical half-width of their Gaussian envelope shape. Using (5) and BMS's relation $h = \sqrt{2}H$ between H and the vertical depth h over which strong, observable mixing occurs, it is found that (5) implies that if $h > 65$ m, then little back-reflection occurs. This size for h is fairly small compared to the most important CAT events (e.g., Browning and Watkins 1970); and hence back-reflection is most likely not a strong constraint on the CAT-induced momentum flux into the mesosphere.

b. Dissipation of inertia-gravity waves by viscous diffusion and radiative damping

The mean viscous energy-dissipation rate per unit mass and unit time for an inertia-gravity wave with wavenumber vector $\mathbf{k}$ is approximated by substituting the plane inertia-gravity wave solution of the Boussinesq model into the usual expression for the viscous energy dissipation rate in a nondivergent flow [cf. (16.3) in Landau and Lifshitz 1987]. The result is

$$\nu|\mathbf{k}|^2\overline{|\mathbf{u}|^2} = \nu|\mathbf{k}|^2 E\left(1 + f^2/\hat{\omega}^2\frac{N^2 - \hat{\omega}^2}{N^2 - f^2}\right) \qquad (6)$$

$$\cong \nu|\mathbf{k}|^2 E(1 + f^2/\hat{\omega}^2). \qquad (7)$$

Here $\mathbf{u} = (u, v, w)$ are the wave velocities, $E \equiv \frac{1}{2}(\overline{|\mathbf{u}|^2} + \overline{\sigma^2/N^2})$ is the standard mean intrinsic wave energy density per unit mass given in terms of wave velocities and density disturbance σ (cf. BMS for details on the wave structure), and the kinematic viscosity ν due to molecular diffusion will be modeled as

$$\nu = \nu_0 \exp[+(z - z_0)/H_s], \qquad (8)$$

where H_s is the density-scale height. For the ray tracing, (8) has been used with $H_s = 7$ km and $\nu_0 = 10^{-4}$ m^2 s^{-1} at $z_0 = 15$ km in the second, approximate form in (7), which is uniformly accurate for all $\hat{\omega}$, with very small relative error $O(f^2/N^2)$.

The factor $|\mathbf{k}|^2$ in (7) shows how viscous dissipation acts more strongly on waves with smaller wavelength, and the factor $(1 + f^2/\hat{\omega}^2)$ shows how viscous dissipation acts stronger on low-frequency than on high-frequency waves. The latter effect arises because inertia-gravity waves do not obey energy equipartition; that is, for these waves potential energy/kinetic energy $\cong (1 - f^2/\hat{\omega}^2)/(1 + f^2/\hat{\omega}^2)$.

The temperature disturbance associated with the gravity waves upsets the radiative transfer equilibrium of the stable background temperature field and this induces radiative transfer processes that seek to dampen the waves with a damping timescale $1/\hat{\alpha}$, which depends on both the altitude and on the vertical wavenumber m of the wave packet. The damping term appears in the linearized buoyancy equation as

$$\sigma_t + N^2 w = -\hat{\alpha}\sigma; \qquad (9)$$

and hence the mean radiative energy-dissipation rate per unit mass and unit time for an inertia-gravity wave is

$$\hat{\alpha}\overline{(\sigma^2/N^2)} = \hat{\alpha}E\left(1 - f^2/\hat{\omega}^2\frac{N^2 - \hat{\omega}^2}{N^2 - f^2}\right)$$

$$\cong \hat{\alpha}E(1 - f^2/\hat{\omega}^2). \qquad (10)$$

The parametrization of $\hat{\alpha}$ used for the ray tracing was a simplified version of the radiative transfer code "MID-RAD" used by Haynes and Ward (1993) (and based originally on Shine 1987; Fels and Schwarzkopf 1981;

TABLE 1. Parameters for ray-tracing sample runs and transmission coefficients.

Wave packet	$k_0h = 0.014$		$m_0/k_0 = -170.$ $N = 0.015\ s^{-1}$
	h (m)	f/N	Transmission coefficient
(a)	35	0.01	0.00
(b)	70	0.01	0.81
(c)	35	0	0.00
(d)	70	0	0.68

Schwarzkopf and Fels 1985), whose details are given in the appendix.

The factor $(1 - f^2/\hat{\omega}^2)$ in (10) highlights the important fact that radiative damping acts only very weakly on low-frequency inertia-gravity waves, because these waves have comparatively little potential energy. In other words, low-frequency inertia–gravity waves are almost "invisible" to radiative damping. This fact that at first sight seems counterintuitive will prove of crucial importance for the ray-tracing results that follow.

c. Ray-tracing equations

The standard ray-tracing formalism (cf. Andrews et al. 1987, p. 215) is generated by the absolute frequency function

$$\Omega(z, k, m) \equiv +\sqrt{\left(N^2\frac{k^2}{k^2 + m^2} + f^2\right)} + U(z)k, \quad (11)$$

in which, for simplicity, the term $f^2m^2/(k^2 + m^2)$ in the intrinsic frequency part has been replaced by f^2 with uniform small relative error $O(f^2/N^2)$. The group-velocity ray $x(t)$, $z(t)$, and the rate of change of the slowly varying wavepacket parameters $k(t)$, $m(t)$, and $\omega(t)$ along a ray are then given by the standard ray-tracing equations:

$$\frac{d_g}{dt}(x, z) \equiv +\left(\frac{\partial\Omega}{\partial k}, \frac{\partial\Omega}{\partial m}\right)$$

$$= \frac{\hat{\omega}^2 - f^2}{\hat{\omega}}\frac{(m^2/k, -m)}{k^2 + m^2} + (U(z), 0) \quad (12)$$

$$\frac{d_g}{dt}(k, m) \equiv -\left(\frac{\partial\Omega}{\partial x}, \frac{\partial\Omega}{\partial z}\right) = (0, -U_z(z)k) \quad (13)$$

$$\frac{d_g\omega}{dt} \equiv +\frac{\partial\Omega}{\partial t} = 0, \quad (14)$$

where $\hat{\omega} = \omega - U(z)k$ is the intrinsic frequency, and d_g/dt denotes time differentiation along a group-velocity ray. Corresponding to the symmetries of Ω with respect to x and t there are two first integrals $k = k_0$ and $\omega = \omega_0$.

The wave amplitude evolution along nonintersecting rays can be computed to leading order using the standard conservation equation for the spatial density of wave action $\rho E/\hat{\omega}$ [e.g., (4.A11)–(4.A13) in Andrews et al. (1987), where their E is our ρE]. However, $\rho E/\hat{\omega}$ changes not only because of wave dissipation, but also in response to the focusing–defocusing of a bundle of adjacent rays as described by $\nabla \cdot \mathbf{c}_g$. This effect is irrelevant for the total flux of wave action into the mesosphere, provided only that the rays in question do eventually reach the mesosphere.

On the other hand, the Hamiltonian structure of the ray-tracing equations (12)–(13) implies that the joint spatial–spectral volume element $dx\ dz\ dk\ dm$ is invariant along rays, that is, $d_g(dx\ dz\ dk\ dm)/dt = 0$. Because of this, a joint spatial–spectral wave-action density $n(x, z, k, m, t)$ can fruitfully be used here. This n is formally related to the spatial wave-action density by

$$\rho\frac{E}{\hat{\omega}} \equiv \int_{-\infty}^{+\infty}\int_{-\infty}^{+\infty} n(x, z, k, m, t)\ dk\ dm. \quad (15)$$

Demanding that wave-action conservation holds for each spectral element separately then immediately implies, for nondissipating waves, that

TABLE 2. Transmitted percentage of emitted pseudomomentum spectrum as a function of layer depth h, Prandtl ratio f/N, and relative mixing strength of velocity and potential temperature $\alpha/(\beta\sqrt{Ri})$. The values for emitted $\mathcal{P}_*^t$ are taken from Table 2 in BMS.

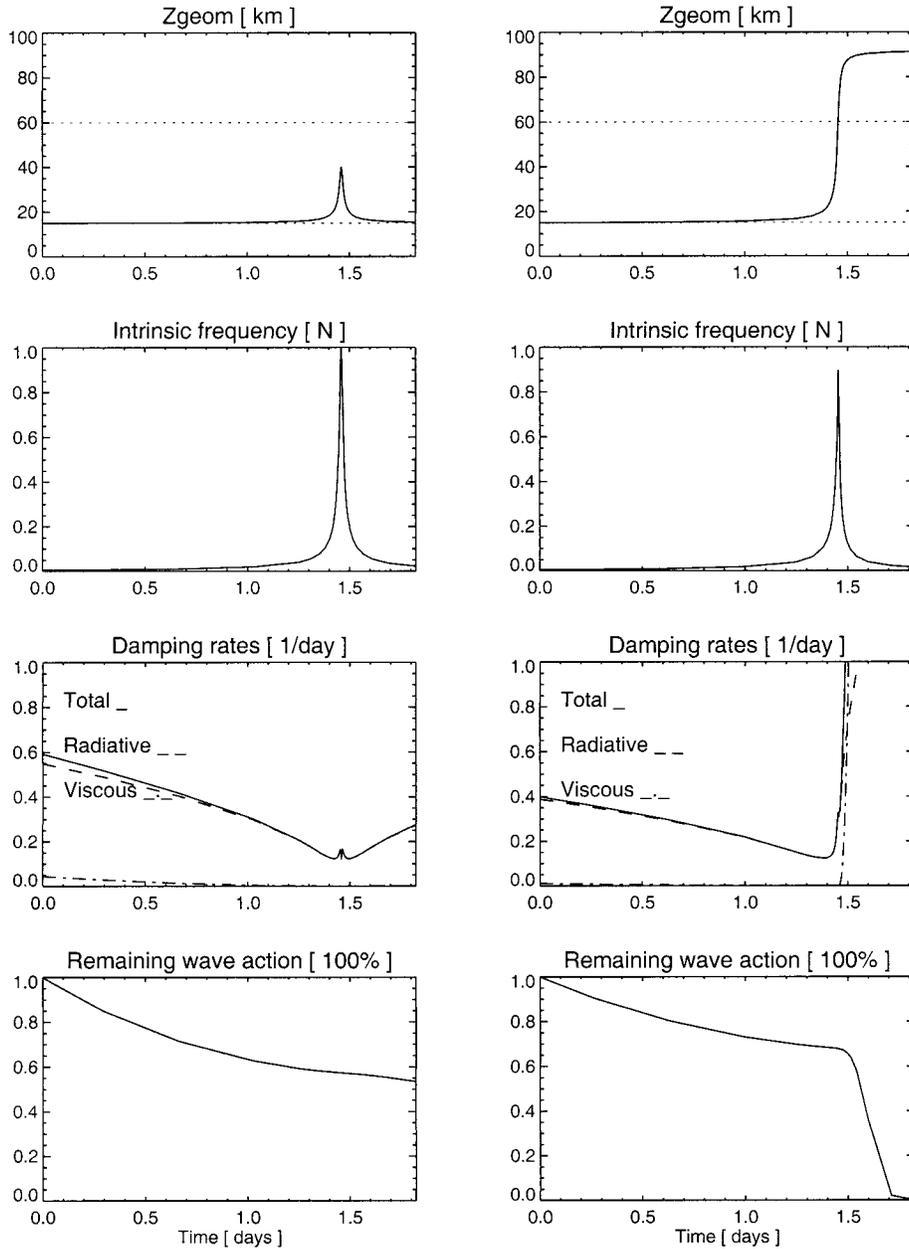| f/N	$\dfrac{\alpha}{(\beta\sqrt{Ri})}$	Emitted $\mathcal{P}_*^t$	$h = 50$ m	$h = 100$ m	$h = 200$ m
0.0	0.0	0.40	0.07 = 18%	0.18 = 45%	0.24 = 60%
0.0	0.5	0.40	0.07 = 18%	0.18 = 45%	0.24 = 60%
0.0	1.0	0.40	0.07 = 18%	0.18 = 45%	0.24 = 60%
0.005	0.0	0.12	0.02 = 18%	0.07 = 61%	0.10 = 86%
0.005	0.5	0.14	0.03 = 21%	0.09 = 62%	0.12 = 85%
0.005	1.0	0.17	0.04 = 24%	0.11 = 63%	0.14 = 84%
0.01	0.0	0.05	0.0065 = 13%	0.029 = 58%	0.045 = 90%
0.01	0.5	0.07	0.014 = 19%	0.043 = 62%	0.063 = 90%
0.01	1.0	0.10	0.024 = 24%	0.066 = 66%	0.089 = 89%

FIG. 3. Ray-tracing results. Rotation $f/N = 0$. (left) Packet (c) with $h = 35$ m; (right) packet (d) with $h = 70$ m.

$$\frac{d_g(n \; dx \; dz \; dk \; dm)}{dt} = 0 \Rightarrow \frac{d_g n}{dt} = 0. \qquad (16)$$

Adding dissipation terms on the right-hand side then results finally in

$$\frac{d_g n}{dt} = -n[\hat{\alpha}(z, m)(1 - f^2/\hat{\omega}^2)$$

$$+ \; \nu(z)(k^2 + m^2)(1 + f^2/\hat{\omega}^2)]. \qquad (17)$$

Here $\hat{\alpha}(z, m)$ is given by the parametrization described in the appendix and $\nu(z)$ is given by (8). Because k is

constant along rays, the relative damping of wave action describes equally well the relative damping of pseudomomentum. Also, the ray-tracing equation for $x(t)$ is decoupled from the other equations and, hence, only $z(t)$, $m(t)$ and $\hat{\omega}(t)$ will be considered from now on.

Four typical ray-tracing runs for type-I, upward–eastward waves are now presented. The initial wavenumbers k_0 and m_0 are chosen near the maximum of the spectral pseudomomentum density that corresponds to the class of mixed-layer initial conditions investigated by BMS (cf. their Fig. 5). The Coriolis parameter

f and the vertical depth h of the corresponding mixed layer have been chosen as summarized in Table 1. All rays are launched at $z = 15$ km and their remaining wave action is measured when they cross $z = 60$ km, which is taken to mark their entry into the mesosphere. If the rays are back-reflected before reaching that altitude, then their wave action at $z = 60$ km is reckoned as 0. Without loss of generality the wave-action density $n = 1$ initially, and the transmission coefficient is hence equal to the value of n when the ray crosses 60-km altitude. The zonal mean velocity profile (Fig. 1 in BMS) is approximated by piecewise linear segments joining the points

$$U[\text{m s}^{-1}] = [0, 20, -50, 0]$$

$$z[\text{km}] = [0, 10, 60, 85], \tag{18}$$

and the ray-tracing results are illustrated in Figs. 2 and 3.

The smaller waves [(a) and (c)] are back-reflected while the larger waves [(b) and (d)] reach the mesosphere. The presence of background rotation in (a) and (b) noticeably reduces the radiative damping strength compared with the nonrotating (c) and (d). Two very different stages in the evolution of the rays can be distinguished. In the first stage $|m| \gg |k|$; and hence the vertical group velocity is very small and the waves spend a long time near their launch altitude. The duration of this first, "dormant" stage can be estimated by the time required for the mean shear to reduce the vertical wavenumber m of the waves to 0, which gives $|U_z k_0/m_0|^{-1} \approx 1.5$ days. However, once $|m| \sim |k|$, the vertical group velocity becomes very large and the waves now undergo a second, rapid ascent stage. The maximal vertical group velocity can be estimated from (12) to occur when $2m^2 \approx k^2$, which gives $w_g \approx 0.38N/k \approx 30$ m s^{-1} for $h = 70$ m.[2] In a fraction of a day this rapid ascent leads to either back-reflection of the waves or to their transmission to the mesosphere.

d. Transmission of mixed-layer wave spectrum

The pseudomomentum transmission coefficients can be calculated for each component of the emitted wave spectrum from mixed layers investigated by BMS. This yields a transmission matrix, with entries analogous to those in Table 1, in which only type-I, eastward–upward waves can have nonzero transmission coefficients. Multiplying the emitted pseudomomentum spectrum [i.e., the spectral density appearing in (27) of BMS] component by component by this transmission matrix and

then summing over all components gives the total pseudomomentum that actually reaches the mesosphere.

This calculation has been done for the two-dimensional cases studied in BMS, and the relevant parameters and results are presented in Table 2. The total amount of emitted pseudomomentum due to type-I waves is given by the nondimensional diagnostic $\mathcal{P}^I_*$ as defined by (27) and (28) in BMS. The mixing parameters α and β range from 0 to 1 and measure the extent to which the background gradients of zonal velocity and potential temperature have been eroded in the mixed layer. The magnitudes of these background gradients are $N/\sqrt{\text{Ri}}$ and N^2, respectively, where Ri is the background Richardson number. As noted in BMS, the diagnostic $\mathcal{P}^I_*$ depends only on $\alpha/(\beta\sqrt{\text{Ri}})$ and on Prandtl's ratio f/N. The vertical depth of the mixed layer h does not affect $\mathcal{P}^I_*$ but it strongly affects the transmitted percentage of the wave spectrum; and hence three different values of h have been considered. In all cases, the vertical/horizontal aspect ratio of the mixed layer was held fixed at 0.01.

The results in Table 2 show a strong increase in transmitted percentage with increasing h and with increasing Prandtl ratio f/N. Eventually, transmission becomes almost perfect in the case $h = 200$ m and $f/N = 0.01$. These trends arise because increasing h limits the importance of back-reflection and increasing f/N limits the effectiveness of radiative damping, as was noted qualitatively before. By comparison, the importance of the relative mixing strength $\alpha/(\beta\sqrt{\text{Ri}})$ is slight.

Based on these results, it can be expected that a mixed layer with $h \geq 100$ m and with vertical/horizontal aspect ratio $\leq f/N$ will emit type-I waves that are transmitted almost perfectly to the mesosphere. (If the aspect ratio $\gg f/N$, then roughly only half of the emitted pseudomomentum reaches the mesosphere.) To judge this conclusion, it is important to note that the total *dimensional* pseudomomentum is proportional to the fourth power of the vertical depth of the mixed layer (cf. BMS), which means that mixed layers with large h are much more important for pseudomomentum emission than those with small h. Hence, back-reflection and radiative damping turn out to be quite ineffective filtering mechanisms: both act most strongly on the emitted waves from small (and therefore weak) mixed layers, while allowing the emitted waves from large (and therefore strong) mixed layers to propagate almost without attenuation to the mesosphere.

3. Ensemble of stratospheric CAT events

The mean zonal stress on the mesosphere due to gravity waves induced by stratospheric CAT events can be calculated by considering an ensemble of many individual CAT events that occur randomly in space and time. The individual pseudomomentum contributions from each CAT event can be added up if different CAT events emit mutually incoherent wave trains. This will

---

[2] The formal validity of the WKB approximation may well break down during the rapid ascent stage. One relevant WKB parameter is $|m(t)^{-2} dm(t)/dz(t)|$, which measures the relative rate of change of $m(t)$ along a ray and which ought to be small for formal validity of WKB (cf. Lighthill 1978, p. 324). It turned out that this parameter becomes $O(1)$ during the rapid ascent stage, which points to the need for a refined theory to calculate detailed wave amplitudes, etc., during this stage.

be the case if the spatial occurrence of the CAT events is sufficiently random. In addition, the vertical mean shear also acts as a very efficient randomizer of wave phase. The relevant statistics of the CAT ensemble must be deduced either from observations or from a reasonably complete theoretical model of CAT generation. Neither approach has led to reliable CAT statistics at present; and hence any calculation of CAT-induced momentum flux into the mesosphere can at present only give a rough, order-of-magnitude estimate of it.

a. Formula for CAT-induced mesospheric stress

Consider now an ensemble of CAT events in the summer stratosphere. For simplicity, attention is focused on a typical region of increased mean shear between the troposphere jet-stream maximum and the zero-wind line above (cf. Fig. 1 in BMS). This region has a vertical depth H_{CAT} of about 5–10 km. Let γ be the average volume fraction that contains CAT in its actively turbulent, and hence most detectable, state at any given time. Typical observational estimates of γ are a couple of percent (e.g., Dewan 1981a; Ludlam 1967, 1980, and references therein). The same observations give an estimate of the duration τ of the actively turbulent phase of a single CAT event of tens of minutes. The vertical depth h and horizontal width b that is occupied by detectable turbulence in a CAT event is observed to be $O(100 \text{ m})$ and $O(10 \text{ km})$, respectively. The vertical depth h can be taken as the relevant vertical mixing length for an individual CAT event. Together, the above CAT parameters determine the total CAT-event rate, that is, the number of new CAT events occuring in the slab of depth H_{CAT} per unit time. This number (per unit horizontal area) is

$$\approx \gamma \frac{H_{\mathrm{CAT}}}{\tau h b^2}, \tag{19}$$

where hb^2 is the approximate volume occupied by the detectable turbulence of a single CAT event.

Multiplying this CAT-event rate with the single-event pseudomomentum that reaches the mesosphere then gives the total CAT-induced mesospheric zonal stress. This single-event pseudomomentum is given by a transmission coefficient Tr times the emitted upward–eastward pseudomomentum. Using BMS's nondimensional pseudomomentum emission quantity $\mathcal{P}_*^l$ [as defined in their (28)], the single-event pseudomomentum can be written as

$$\approx \mathrm{Tr}\mathcal{P}_*^l \frac{\sqrt{2}\rho_0 \mathcal{E}_0}{hN}, \tag{20}$$

where $\rho_0 \mathcal{E}_0$ is the total disturbance energy produced by the mixing inside a CAT event. The mixing erodes the background gradients of potential temperature and zonal velocity (with respective values for the mixing param-

eters β and α) over the vertical mixing length h inside the CAT event; and hence $\mathcal{E}_0$ can be approximated as

$$\mathcal{E}_0 \approx b^2 N^2 (\alpha^2 \mathrm{Ri}^{-1} + \beta^2) \int_{-h/2}^{+h/2} \frac{z^2}{2} \, dz$$

$$= \frac{1}{24} h^3 b^2 N^2 (\alpha^2 \mathrm{Ri}^{-1} + \beta^2), \tag{21}$$

where $\mathrm{Ri} = N^2/(U_z)^2$ is the background Richardson number.[3]

The total CAT-induced mesospheric zonal stress, say, S_{CAT}, is then given by the product of (19) and (20), using (21). This yields

$$S_{\mathrm{CAT}} \approx \rho_0 \frac{\gamma H_{\mathrm{CAT}}}{\tau} hN\mathrm{Tr}\mathcal{P}_*^l \frac{\sqrt{2}}{24} (\alpha^2 \mathrm{Ri}^{-1} + \beta^2). \tag{22}$$

Appropriate values for $\mathrm{Tr}\,\mathcal{P}_*^l$ can be retrieved from the entries in Table 2. Typically, $\mathrm{Tr}\,\mathcal{P}_*^l \approx 0.05$–$0.1$. Note that this estimate is proportional to γ/τ [cf. (19)] and proportional only to the first power of h, as contrasted with the fourth power for a single layer noted at the end of section 3c of BMS.

b. Rough upper bound on mesospheric zonal stress

The case of perfect mixing $\alpha = \beta = 1$ is now used to generate a rough upper bound on S_{CAT}, using plausible estimates of the other physical parameters. We regard this as an upper bound because real mixing is often less than perfect; a recent reference is Alisse and Sidi (1999). The details are collected in Table 3. Substitution in (22) gives

$$S_{\mathrm{CAT}} \lesssim 10^{-3} \text{ N m}^{-2}. \tag{23}$$

It happens that this estimate of S_{CAT} is of the same order as commonly inferred values for the globally averaged zonal momentum flux into the summer mesosphere that is necessary to produce realistic jet closures in GCMs. Taken literally, (23) would then imply that a significant part of that momentum flux could be due to gravity waves induced by stratospheric CAT events. However, we must remember that (23) is only a rough upper bound. Furthermore, the extreme uncertainties inherent in our assumptions about the "typical" CAT ensemble in Table 3 must be noted. Therefore, at present it seems more prudent to conclude only that CAT-induced contributions to the mesospheric angular momentum budget cannot safely be neglected.

4. Concluding remarks

The potential relevance for the mesospheric angular momentum of S_{CAT}, as indicated by the rough upper

---

[3] Alternatively, the specific initial conditions of BMS could be used here, but this would lead to a numerically very close expression for $\mathcal{E}_0$.

TABLE 3. Parameters for rough upper bound estimate of S_{CAT}. Note that the envelope half-width scales (H, L) used in BMS are related to (h, b) by $(H, L) = (h, b)/\sqrt{2}$.

Quantity	Symbol	Value
Mass density at 15-km altitude	ρ_0	0.21 kg m^{-3}
Buoyancy frequency	N	0.015 s^{-1}
Prandtl's ratio	f/N	0.01
Background Richardson number	Ri	1.0
Vertical depth of lower stratosphere with strong CAT activity	H_{CAT}	7000 m
Average volume fraction containing active, detectable turbulence	γ	0.03
Lifetime of active, detectable turbulence of a single CAT event	τ	1500 s
Vertical depth of well-mixed core of a single CAT event	h	200 m
Horizontal width of well-mixed core of a single CAT event	b	20 000 m
Velocity and potential temperature mixing efficiencies	(α, β)	(1, 1)
$\mathcal{P}_*^l$ for $f/N = 0.01$, $h/b = 0.01$, and $\alpha/\beta = 1$	$\mathcal{P}_*^l$	0.10
Transmission coefficient	Tr	0.9

bound (23), makes it important to notice clearly the limitations of the transmission calculations and the ensemble estimates put forward in this paper. The ray-tracing calculation for the stratospheric wave transmission is arguably a robust part of the approach. Its extension to three-dimensional mean-flow variability and/or mean-flow time dependence would be conceptually straightforward.

The situation is much worse with regard to reliable CAT ensemble statistics. Typical CAT mixing parameters α and β, for momentum and mass, respectively, are at present poorly known. Yet they enter directly into any estimate for S_{CAT}. The large observational uncertainties with respect to typical values of α and β, of typical layer depth h, and of actively turbulent volume fraction γ underline the need for further observational and theoretical studies. Further progress would benefit not only estimates of CAT-induced momentum fluxes, but might also put within reach the parameterization of an intimately related problem relevant in both the atmosphere and the oceans: namely, the problem of CAT-induced small-scale vertical diffusion of tracers (e.g., Dewan 1981b).

APPENDIX

Parametrization of Radiative Damping Rate

The version of MIDRAD used here parameterizes accurately the infrared damping due to CO_2 between 20- and 90-km altitude for vertical wavenumbers up to ~ 1 km^{-1}, while giving a slight overprediction of $\hat{\alpha}$ for larger vertical wavenumbers (cf. Haynes and Ward 1993). Let z^* be altitude (in km), $T^*(z^*)$ temperature (in degrees Kelvin), and m^* the vertical wavenumber (in km^{-1}); then the damping rate $\hat{\alpha}$ is given by

$$\hat{\alpha} = \frac{1}{\text{days}}\left(\frac{960}{T^*}\right)^2 \exp(-960/T^*)[a(z^*) + b(z^*)\sqrt{|m^*|}],$$
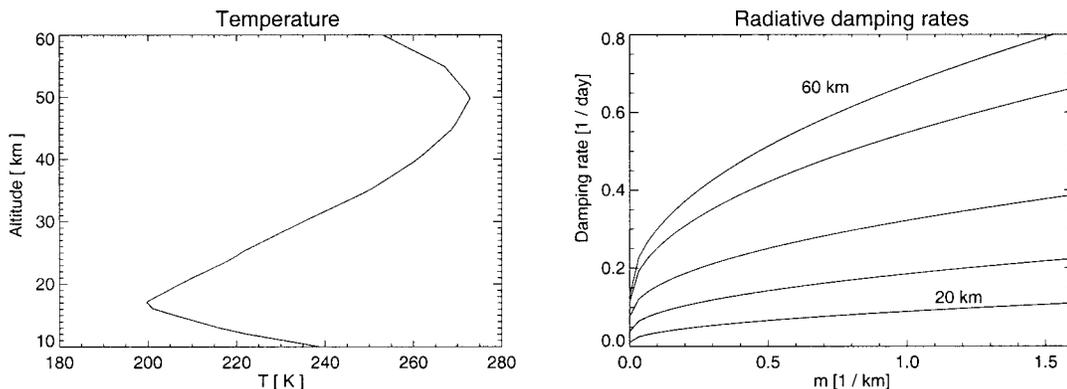
(A1)

FIG. A1. Temperature profile and radiative damping rate as a function of vertical wavenumber, at different altitudes (20, 30, 40, 50, 60 km).

where

$$a(z^*) = 0.422 + 0.001625(z^* - 62.5)$$
$$- 0.007125\sqrt{1 + (z^* - 62.5)^2} \quad (A2)$$
$$b(z^*) = 0.646 + 0.032(z^* - 39.5)$$
$$+ 0.018\sqrt{9 + (z^* - 39.5)^2}. \quad (A3)$$

The parameterized $\hat{\alpha}(m)$ at various altitudes is plotted in Fig. A1 together with the corresponding summer standard temperature profile (cf. Andrews et al. 1987, p. 72).

REFERENCES

Alisse, J. R., and C. Sidi, 1999: Experimental probability density functions of small-scale fluctuations in the stably stratified atmosphere. *J. Fluid Mech.,* in press.

Andrews, D. G., J. R. Holton, and C. B. Leovy, 1987: *Middle Atmosphere Dynamics.* Academic Press, 489 pp.

Browning, K. A., and C. D. Watkins, 1970: Observations of clear air turbulence by high power radar. *Nature,* **227,** 260–263.

Bühler, O., M. E. McIntyre, and J. F. Scinocca, 1999: On shear-generated gravity waves that reach the mesosphere. Part I: Wave generation. *J. Atmos. Sci.,* **56,** 3749–3763.

Dewan, E. M., 1981a: Vertical transport by small-scale stratospheric turbulence: A critical review. Air Force Geophysics Lab, Hanscom AFB, Rep. AFGL-TR-81-0051, 32 pp. [NTIS ADA 087434.]

——, 1981b: Turbulent vertical transport due to thin intermittent mixing layers in the stratosphere and other stable fluids. *Science,* **211,** 1041–1042.

Fels, S. B., and M. D. Schwarzkopf, 1981: An efficient, accurate algorithm for calculating CO_2 15mm band cooling rates. *J. Geophys. Res.,* **86,** 1205–1232.

Haynes, P. H., and W. E. Ward, 1993: The effect of realistic radiative transfer on potential vorticity structures, including the influence of background shear and strain. *J. Atmos. Sci.,* **50,** 3431–3453.

Landau, L. D., and E. M. Lifshitz, 1987: *Fluid Mechanics.* 2d ed. Pergamon, 539 pp.

Lighthill, M. J., 1978: *Waves in Fluids.* Cambridge University Press, 504 pp.

Ludlam, F. H., 1967: Characteristics of billow clouds and their relation to clear-air turbulence. *Quart. J. Roy. Meteor. Soc.,* **93,** 419–435.

——, 1980: *Clouds and Storms: The Behavior and Effect of Water in the Atmosphere.* The Pennsylvania State University Press, 405 pp.

Schwarzkopf, M. D., and S. B. Fels, 1985: Improvements to the algorithm for computing CO_2 transmissivities and cooling rates. *J. Geophys. Res.,* **90,** 10 541–10 550.

Shine, K. P., 1987: The middle atmosphere in the absence of dynamical heat fluxes. *Quart. J. Roy. Meteor. Soc.,* **113,** 603–633.